

Prostate Cancer Detection: Fusion of Cytological and Textural Features

Kien Nguyen¹, Anil K. Jain¹, and Bikash Sabata²

¹ Department of Computer Science and Engineering, Michigan State University

{nguye231, jain}@cse.msu.edu

² Ventana Medical System, Inc.

Bikash.Sabata@bioimagene.com

Abstract. A computer assisted system for histological prostate cancer diagnosis can assist pathologists in two stages: (i) to locate cancer regions in a large digitized tissue biopsy, and (ii) to assign Gleason grades to the regions detected in stage 1. Most previous studies on this topic have primarily addressed the second stage by classifying the pre-selected tissue regions. In this paper, we address the first stage by presenting a cancer detection approach for the whole slide tissue image. We propose a novel method to extract a cytological feature, namely the presence of cancer nuclei (nuclei with prominent nucleoli) in the tissue, and apply this feature to detect the cancer regions. Additionally, conventional image texture features which have been widely used in the literature are also considered. The performance comparison between the proposed cytological-textural feature combination method with the texture only based method demonstrates the robustness of the extracted cytological feature. At a false positive rate of 4.6%, the proposed method is able to achieve a sensitivity of 71% on a dataset including 6 training images (each of which has approximately $4,000 \times 7,000$ pixels) and 11 whole slide test images (each of which has approximately $5,000 \times 23,000$ pixels). All images are at $20 \times$ magnification.

1 Introduction

In a typical procedure of histological prostate cancer diagnosis, a pathologist obtains a tissue sample from a prostate biopsy and treats it by a staining protocol to highlight the histological structures (e.g. H&E staining [1]). State of the art slide scanners can capture the content of the entire sample slide and create one whole slide image at any magnification. However, with a high magnification slide image (which may contain approximately $10,000 \times 50,000$ pixels at $40 \times$), it is time-consuming for pathologists to investigate the tissue structures and diagnose the cancer. Thus, there is a need to build a computer-aided system to assist pathologists in detecting and grading the cancer.

Gleason grading [2] is a well-known method to determine the severity of prostate cancer. In this method, only the gland structures and morphology are considered to assign a grade from 1 to 5 to the cancer region. Grade 1 is the least severe and grade 5 is the most severe. Gleason grading method is appropriate for a low magnification image ($\leq 10 \times$), where the details of the tissue elements (nuclei, cytoplasm) are not available. Nguyen et al. [3] obtained good classification results based on the glandular structural features to classify the $10 \times$ magnification images. However, for a more detailed examination, a pathologist would like to examine the tissue at a higher magnification ($20 \times$ or $40 \times$) and utilize cytological features [4] of the tissue (Figures 1a,1b). Cytological features refer to shape, quantity, and arrangement of the basic elements of the tissue such as cell, cytoplasm, and nucleus.

Most of the studies on automated prostate cancer diagnosis utilize various textural

and structural features to classify a small region of interest (ROI) into benign (normal) or malignant (cancer) region, or into different grades. These studies are summarized in Table 1. Only a few studies in the literature have addressed the cancer detection problem in the whole slide image. In [5], the authors performed cancer detection on a whole-mount histological section of size $2 \times 1.75 \text{ cm}^2$ at a low resolution ($8 \mu\text{m}$ per pixel), which created a $2,500 \times 2,200$ image. Glands were segmented by a region growing algorithm initialized at the lumina. Gland size was the only feature used to assign an initial label (cancer or normal) to the gland. Next, a probabilistic pairwise Markov model was proposed to refine the initial gland labels using the labels of neighboring glands. They obtained 87% sensitivity and 90% specificity on a dataset of 40 images. However, it is necessary to notice that lumina are not always present in the cancer regions (for example, lumina can be occluded by mucin or cytoplasm in some cases). As a consequence, gland segmentation algorithm using lumina is not always applicable. Doyle et al. [6] developed a boosted Bayesian system to identify prostate cancer in $40 \times$ whole slide images ($10,000 \times 50,000$ pixels) at multiple resolutions. On a dataset of 100 images at three different resolutions, they obtained the following results (with resolution from low to high): 69%, 70%, and 68% for accuracy, and 0.84, 0.83, 0.76 for area under the ROC curve. As can be seen from these results, the accuracy dropped when the authors used higher resolution images. The reason is that, when creating ground truth for cancer regions of histology images, pathologists commonly annotate a heterogeneous region comprising multiple neighboring cancer glands and intervening normal structures like stroma. At a high resolution, the intervening normal structures (which are annotated as a part of cancer regions) become more salient and are easily classified as normal regions. This can somewhat explain why the accuracies in [5] are higher than the accuracies in [6] although different datasets were used for their experiments. Finally, the whole slide analysis is significantly more complex than the ROI analysis because of the scale of operations that needs to be done. The data sizes are 2 to 3 orders of magnitude more for a whole slide as compared to a ROI. In summary, cancer detection in high magnification whole slide tissue image is still a challenging problem. By observing the cancer detection procedure adopted by pathologists, we establish that an important cytological feature, the presence of cancer nuclei (nuclei with prominent nucleoli) (Figure 2a), is an important clue in deciding if a region is cancerous [7, 8]. In this study, we propose an efficient algorithm to extract cancer nuclei and use them in detecting cancer regions in high magnification ($20 \times$) whole slide images (Figure 5). To the best of our knowledge, cytological features have not yet been exploited in the reported studies on automated cancer detection and grading in prostate histology.

In the proposed approach, we first find all the cancer nuclei in the tissue. Then, we divide the image into a grid of patches. For each patch, we compute two types of features (cytological and textural features; Figures 1c,1d), and combine them to classify the patch as normal or cancerous. Finally, neighboring cancer patches are unified into continuous cancer regions.

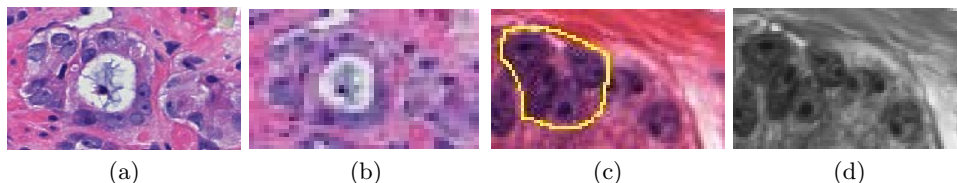


Fig. 1. A tissue image region at (a) $20 \times$ and (b) $5 \times$ magnifications. In the high magnification region, the tissue elements (nuclei, cytoplasm) are clearly visible. Two types of features considered in a tissue region are: (c) cytological feature, which is the presence of cancer nuclei in the region; (d) textural features extracted from the grayscale intensity distribution of the region.

Approach	Dataset	Accuracy
Lumen area and co-occurrence features; classify 100×100 sub-regions into prostatic carcinoma, stroma, and benign tissue [9]	Sub-regions of 8 tissue images (40×)	79.3%
Multiwavelet features; classify images of tissue portions into grade 2, 3, 4, and 5 carcinoma [10]	100 images (100×)	97%
Global and local features; classify 1,600×1,200 images into tumor-nontumor [11]	367 images (20×)	96.7%
Glandular structural features; classify 500×500 images into benign, grade 3, and grade 4 carcinoma [3]	78 images (10×)	88.8%

Table 1. Summary of major studies on ROI classification in automated prostate cancer diagnosis. Since different authors used different datasets, their results cannot be directly compared.

2 Nucleus Segmentation and Classification

2.1 Nucleus Segmentation

To segment nuclei from the tissue area, we propose a maximum object likelihood binarization algorithm. Our goal is to segment an object O with feature vector $f(O)$ in a grayscale image I . We first assume that $f(O)$ follows a density g with parameter vector θ . An estimate $\hat{\theta}$ is obtained from a training set. A threshold t_0 to binarize I is obtained such that the average object likelihood of the foreground blobs is maximized. Formally, let $B_i^t, i = 1, \dots, n^t$, denote the n^t foreground blobs generated by binarizing I with a threshold $t \in [t_{min}, t_{max}]$ (note that B_i^t and n^t depend on t). We choose t_0 such that:

$$t_0 = \operatorname{argmax}_t \frac{1}{n^t} \sum_{i=1}^{n^t} g(f(B_i^t) | \hat{\theta}) \quad (1)$$

where $f(B_i^t)$ is the feature vector of blob B_i^t and $g(f(B_i^t) | \hat{\theta})$ is the object likelihood of blob B_i^t since it estimates how similar the features of B_i^t are to the features of the object of interest O (which have density g with parameter $\hat{\theta}$).

In this procedure, after binarizing I using a threshold $t \in [t_{min}, t_{max}]$, we apply a 4-connectivity connected component algorithm to group foreground pixels (pixels whose intensities are greater than t) into blobs $B_i^t, i = 1, \dots, n^t$. This is followed by computation of blob features, $f(B_i^t)$ (area and circularity), and their average object likelihood, $\frac{1}{n^t} \sum_{i=1}^{n^t} g(f(B_i^t) | \hat{\theta})$. The optimal threshold t_0 , computed in Equation (1), is the threshold resulting in the maximum average object likelihood. The blobs obtained by binarizing I with t_0 are the outputs of the algorithm.

Since nuclei appear as blue in H&E stained images, we apply this algorithm on the b channel (which is normalized to $[0,1]$) of the Lab color space (which best represents the blue color). Here, objects O to be segmented are the nuclei. The feature vector of the nucleus is defined as $f(O) = (a, c)$, where a and c denote the area and circularity of a nucleus, respectively. The circularity is defined as $c = (4\pi a)/p^2$, where p denotes the perimeter of the nucleus. In this problem, we assume that the feature density is bivariate Gaussian $f(O) \sim \mathcal{N}(\hat{\mu}, \hat{\Sigma})$, where $\hat{\mu}$ and $\hat{\Sigma}$ are estimated from a training set of manually segmented nuclei.

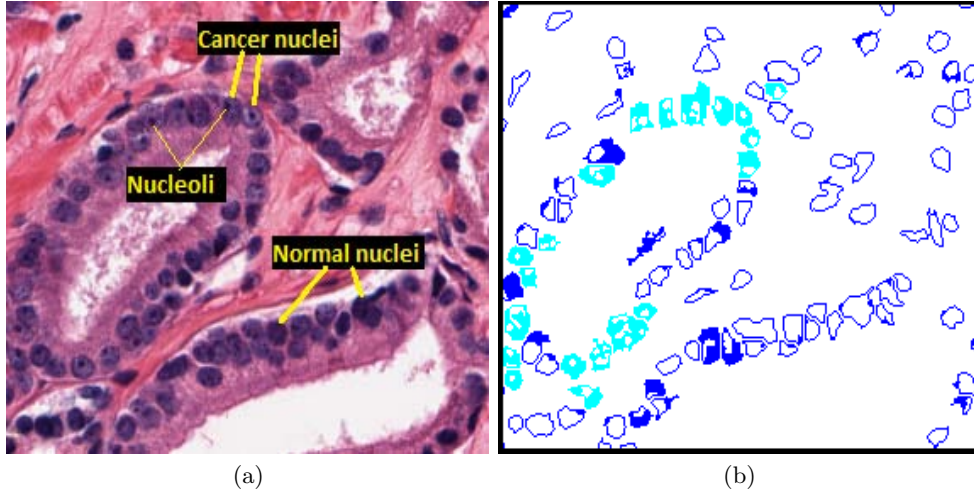


Fig. 2. Nucleus segmentation and classification. (a) Cancer and normal nuclei in a $20\times$ tissue region. (b) Results of the nucleus segmentation and classification. Cyan regions are cancer nuclei and blue regions are normal nuclei. The blank areas inside each nucleus region are the segmented dark spots obtained by the algorithm in section 2.2. In cyan regions, these spots are round and small in size, which are considered nucleoli. In blue regions, these spots are either elongated or much larger in size, which are not considered nucleoli.

2.2 Nucleus Classification

Nuclei in cancer glands ([7, 8]) usually appear light blue and contain prominent nucleoli which appear as small dark spots. On the other hand, nuclei in normal glands usually appear uniformly dark or uniformly light over its entire area without the nucleoli (Figure 2a). We utilize this observation to classify the segmented nuclei into normal or cancer nuclei. First, we segment the dark spots from each nucleus, then the features of these spots are used to determine if the nucleus is a cancer nucleus. These two operations are performed as follows.

(i) Maximum Object Boundary Binarization

By observing that boundaries of the salient objects (dark spots) within a region of interest (nucleus region) typically have strong gradient magnitude, we find a threshold t_0 to binarize the ROI (in a grayscale image) in such a way that it generates the foreground object which has the maximum gradient magnitude on the boundary. Formally, let $O_i^t, i = 1, \dots, n^t$, denote the n^t foreground objects obtained in the ROI, R , when binarizing R with a threshold $t \in [t_{min}, t_{max}]$ (note that O_i^t and n^t depend on t). We choose t_0 such that:

$$t_0 = \operatorname{argmax}_t \left(\max_{i \in [1, n^t]} \operatorname{bound_mag}(O_i^t) \right), \quad (2)$$

where $\operatorname{bound_mag}(O_i^t)$ denotes the average gradient magnitude of the pixels on the boundary of O_i^t .

In this procedure, after binarizing R using a threshold $t \in [t_{min}, t_{max}]$, we use the 4-connectivity property to group foreground pixels (pixels whose intensities are greater than t) into objects $O_i^t, i = 1, \dots, n^t$. Then we compute the average gradient magnitude on the boundary of each object and get the maximum value of these average magnitudes ($\max_{i \in [1, n^t]} \operatorname{bound_mag}(O_i^t)$). The best threshold t_0 , which is computed in Equation (2), is the threshold that maximizes the object boundary gradient magnitude. This is a local binarization method since in each ROI, we find a different threshold t_0 to binarize and

detect the local objects in that ROI.

Since the difference in intensity of the nucleolus and the rest of the nucleus area is most salient in the luminance channel of the image, we apply the algorithm in this channel to segment the dark spots. However, we obtain several spots in each nucleus because some noisy dark regions resulting from the poor tissue staining procedure may also generate spots. Figure 3 shows the result of this binarization.

(ii) Feature-based Object Identification

We need to identify an object of interest O^* (nucleolus) among a pool of objects $\{O_i\}_{i=1}^n$ (dark spots). Similar to the formulation in section 2.1, we estimate the parameters $\hat{\theta}$ of the density g of the feature vector $f(O^*)$ from a training set of manually segmented nucleoli. Then, we choose the object O_m which has the maximum likelihood: $O_m = \operatorname{argmax}_i g(f(O_i)|\hat{\theta})$. The object O_m is considered the object of interest if $f_j^{min} < f_j(O_m) < f_j^{max} \forall j$, where the constraints for each feature, i.e. f_j^{min} and f_j^{max} are estimated from the training set. We again use area and circularity as the features to identify the nucleoli. By using this algorithm, if a nucleolus is found within a nucleus, that nucleus is classified as a cancer nucleus. Otherwise, it is considered a normal nucleus. Figure 2b depicts the results of the nucleus segmentation and classification. For cancer detection purposes, we only keep cancer nuclei and disregard normal nuclei.

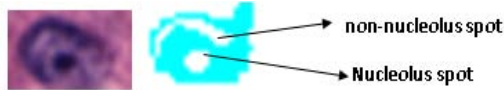


Fig. 3. A cancer nucleus (left) and the segmented dark spots (right). There are two spots detected by the proposed algorithm, one is a true nucleolus and the other is a noisy spot.

3 Textural Features

Similar to [6], the textural features computed for an image patch include first-order statistics, second-order statistics, and Gabor filter features. There are four first-order statistical features comprising mean, standard deviation, median, and gradient magnitude of pixel intensity in the patch. For the second-order statistical features, we form the co-occurrence matrix for all the pixels in the patch and compute 13 features from this matrix [12] which include energy, correlation, inertia, entropy, inverse difference moment, sum average, sum variance, sum entropy, difference average, difference variance, difference entropy, and two information measures of correlation. For the Gabor filter based texture features [13], we create a bank of 10 filters by using two different scales and five different orientations. The mean and variance of the filter response are used as features. Thus, a total of 20 features are extracted by using Gabor filters. We obtain 37 features using these three feature types (4 first-order statistics features, 13 co-occurrence features and 20 Gabor features). By considering texture in each of the three normalized channels of the Lab color space of the image separately, we have a total of $3 \times 37 = 111$ textural features for each patch.

4 Detection algorithm

Since we do not have any prior information (size, shape and boundary) about the cancer regions, we utilize a patch-based approach using a feature set combination method to detect the cancer regions. A grid of patches, each with $S \times S$ pixels, is superimposed

on the image. Let $\{\mathbf{x}_i\}_{i=1}^n$ denote the n sets of features associated with each patch P . Each set \mathbf{x}_i may contain one or more features. We train n classifiers $\{f_i\}_{i=1}^n$, one for each feature set. A patch P is classified as a cancer patch if:

$$\prod_i^n p(f_i(\mathbf{x}_i) = 1) > \prod_i^n p(f_i(\mathbf{x}_i) = 0), \quad (3)$$

where $p(f_i(\mathbf{x}_i) = 0)$ and $p(f_i(\mathbf{x}_i) = 1)$ denote the probability that classifier f_i classifies the feature set \mathbf{x}_i as normal or cancer, respectively. Otherwise, P is considered a normal patch. We apply this algorithm in our problem with two different feature sets ($n = 2$), i.e. cytological feature set and textural feature set. The cytological feature set contains a single feature which is the number of pixels belonging to cancer nuclei in the patch. Both classifiers (f_1 and f_2) used for these two feature sets are Support Vector Machine (SVM) with RBF kernel and $c = 1$. The grid size and placement are chosen based on the method discussed in [6], where the authors superimposed the image with a uniform grid so that the image is divided into 30×30 regions. The reported result using this grid was better than the pixel-based method proposed in the same paper. In a similar manner, we divide the image into 40×40 patches ($S = 40$) and perform patch classification.

Once cancer patches are identified, we create continuous cancer regions by grouping neighboring cancer patches. We divide cancer patches in the image into groups, where each group O contains a set of cancer patches $\{P_i\}_{i=1}^m$ such that $\forall P_i \in O, \exists P_j \in O$, where $d(P_i, P_j) \leq t_d$. Groups with small number of patches are discarded. For each remaining group, we create one continuous cancer region by generating a convex hull of all the patches and set all pixels in this convex hull as cancer pixels. Cancerous tumors are characterized by uncontrolled growth, which makes the spread and shape of the tumor extremely difficult to model. We, therefore, take the most reasonable simplification, i.e. capture the convex hull to get all the cancer regions that may correspond to a single tumor. The grouping process and the removal of small groups (groups with small number of patches) follow the annotation strategy of the pathologist. We can observe in the ground truth that the pathologist only annotates large cancerous regions, including several neighboring cancerous glands but not individual glands. Hence, the minimum size of a group is chosen to be larger than the average size of a cancerous gland.

Many of the assessments made by pathologists are based on a gestalt of the entire region using years of training and experience in evaluating many tissues with cancer. For pathologists, this constitutes their “self evident truth” or heuristics that is usually not documented. The case when a pathologist identifies two neighboring regions as a single region and when he considers them two independent regions is very subjective. With the automated detection and grading research we are engaged in, we hope that some of the subjectivity will be codified and we will have a more consistent review and analysis of cancerous tissues.

5 Experiments

Our dataset contains independent training and test sets. The training set includes 6 images (approximate size is $4,000 \times 7,000$ pixels at $20 \times$ magnification). In each training image, all the cancer glands were marked by a pathologist. In the remaining non-cancerous area, we manually selected a number of training normal regions which contain various benign structures of the tissue (stroma, normal glands with different sizes, normal nuclei). Figure 4a shows part of a training image. The independent test set consists of 11 whole slide images at $20 \times$ magnification (approximate size is $5,000 \times 23,000$ pixels). The difference in size of the training and testing images is not an important issue because what we need for training is the local information of the patches but not the global information of the

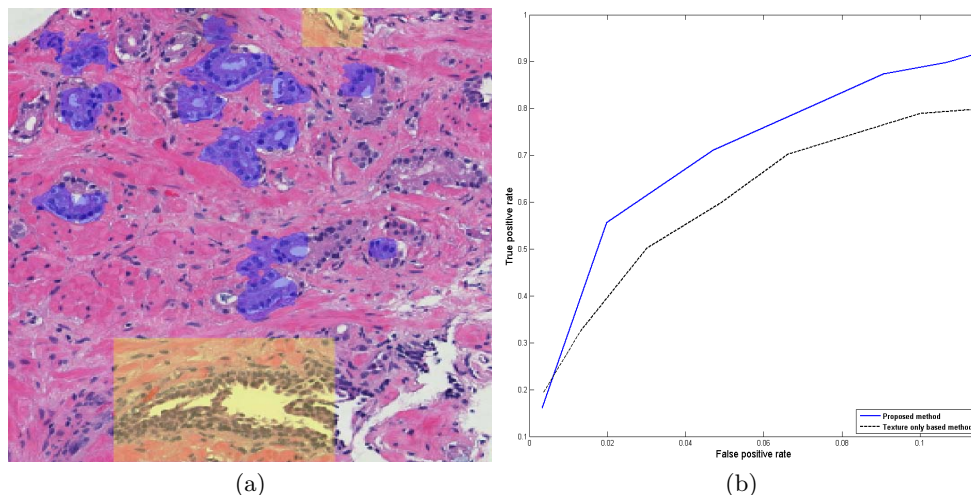


Fig. 4. Experimental results. (a) A region of a training image in which all cancer glands are highlighted in blue and selected normal regions are highlighted in yellow. (b) ROC curves, which plot the average FPR vs TPR over all test images, for the proposed method and the texture only based method obtained by varying the neighboring threshold t_d from 0 pixels to 320 pixels. Note that the scales for TPR and FPR are different.

entire image. The ground truth for the test images (all cancer regions) were also manually labeled by a pathologist. All the non-labeled regions are considered normal. While in the ground truth of the test set, the pathologist annotated the entire cancer region (including neighboring cancer glands and the intervening normal structures such as stroma), only pixels belonging to the cancer glands are annotated as cancer in the training set. In other words, the training data are more reliable.

To evaluate the robustness of the cytological feature, we compare the performance of the proposed feature set combination method with the texture only based method. In the texture only based method, we only use the textural feature set (section 4) and a single classifier (SVM with RBF kernel and $c = 1$) for the detection. For a quantitative comparison, we compute the true positive rate $TPR = TP / (TP + FN)$ and the false positive rate $FPR = FP / (TN + FP)$, where TP, FP, TN, and FN denote the true positive, false positive, true negative, and false negative, respectively, for every test image. The TPR and FPR are then averaged over all test images.

The value of the threshold t_d has a significant influence on both TPR and FPR. Since the training set only includes annotations of cancer glands separately and not the entire cancer region, it is difficult to estimate t_d . Further, it is difficult for a pathologist to tell which value he uses to annotate the cancer region. Hence, it is necessary to test our method with different values of t_d . Figure 4b depicts the ROC curves illustrating the relationship between TPR and FPR obtained by the two methods when t_d is varied from 0 pixels to 320 pixels (a relatively large distance in the image). When t_d increases, both TPR and FPR increase, i.e. there are more true cancer regions being detected while at the same time, more normal regions get incorrectly classified as cancer. For the same FPR, the proposed method always gets a higher TPR than the texture only based method. Since the test set is not large, we choose the best trade-off between TPR and FPR by a qualitative observation of the detection outputs. We determine that for $t_d = 90$ pixels, the proposed method provides the most satisfactory detection results (TPR = 71% at FPR = 4.6%). Figure 5 shows the detection results of the two methods on a whole slide image when $t_d = 90$ pixels and Figure 6 shows a close-up region of the same image for better

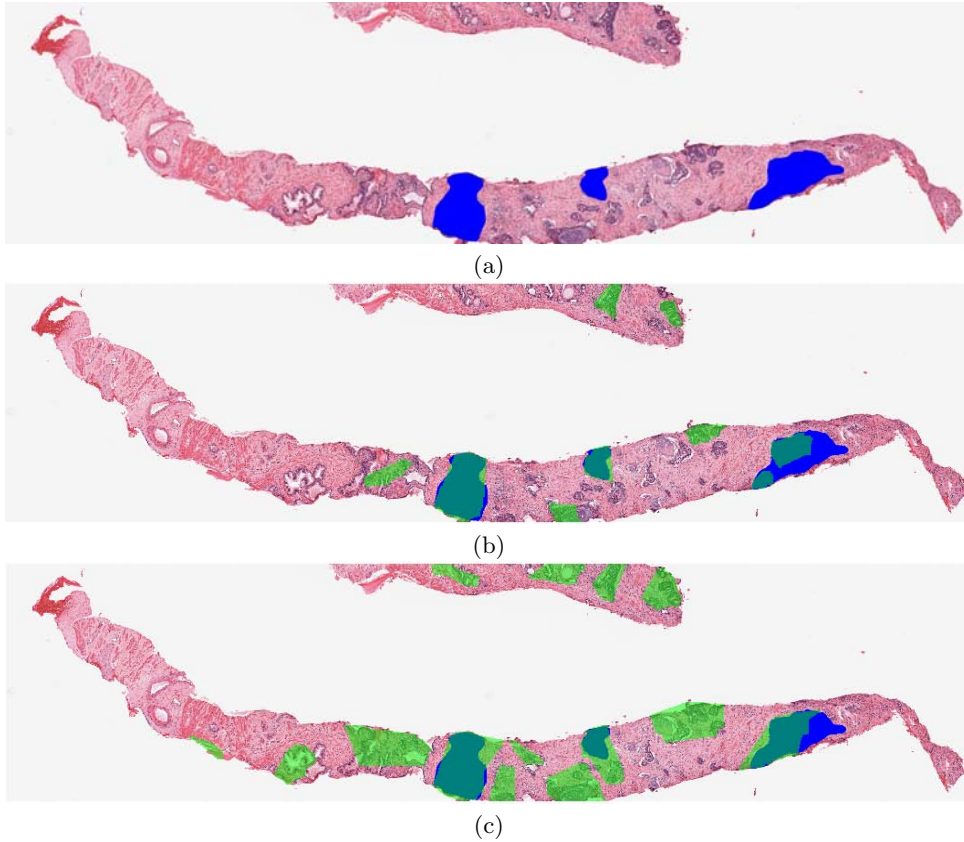


Fig. 5. Detection results on a test image. (a) Input image with cancer regions highlighted in blue by a pathologist (ground truth); (b) result of the proposed method overlaid on the ground truth image (with detected cancer regions highlighted in green); (c) result of the texture only based method overlaid on the ground truth image (with detected cancer regions highlighted in green). $t_d = 90$ pixels is used for both the methods.

details. In this image, both the methods can find most of the cancer regions. However, the proposed method has fewer false detections than the texture only based method.

To save computation time, we perform background removal by using a simple thresholding operation on the L channel of the Lab color space. By doing this, the white area (non-tissue area) is discarded prior to the patch feature extraction. However, to be able to compare our results with [5] and [6] in which the authors did not perform background removal, we use all the image pixels when computing the TPR and the FPR. Although different datasets were used, we can still have an indirect comparison among the three studies. At a TPR of 87% (which was the most satisfactory result in [5]), the FPR obtained by their method was roughly 10%, in [6] it was roughly 28% and in the proposed method it is roughly 8.4%. In the context of this paper, since we use background removal for both the proposed method and the texture only based method and compute the TPR and the FPR for them in the same way, the comparison between these two methods is still valid.

We do not compare our selected features with morphological features because, to compute morphological features, we need to segment complete glands, which is not a trivial task. Since we do not have ground truth for the nucleus segmentation (it is indeed a labor intensive task for pathologists to mark every single nucleus), we only qualitatively evaluate

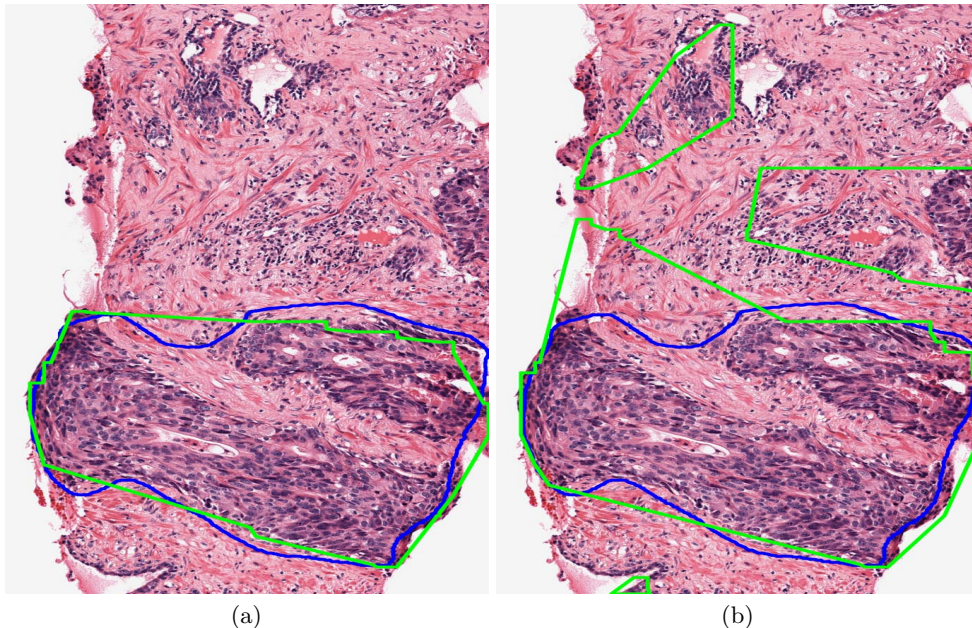


Fig. 6. Detection results of the proposed method (a) and the texture only based method (b) in a close-up region sampled from the image in Figure 5a. The blue contour depicts the annotated cancer region by the pathologist and the green contours depict the outputs by the algorithm.

the proposed nucleus segmentation method by comparing with the popular Otsu's method [14] and a Bayesian classification method which was used in [15]. The Otsu's method is an adaptive thresholding method which is used to create a binary image I_b from a grayscale image I_g . This method assumes that each image pixel belongs to one of the two classes, i.e. foreground and background. Then, it searches for an optimal threshold $t_0 \in [a, b]$, where $[a, b]$ is the intensity range of I_g , to binarize I_g such that the inter-class variance is maximized. The inter-class variance corresponding to a threshold t is computed by

$$\sigma_b^2(t) = \omega_1(t)\omega_2(t)[\mu_1(t) - \mu_2(t)]^2, \quad (4)$$

where ω_1, ω_2 denote the probabilities and μ_1, μ_2 denote the intensity means of the two classes. We apply Otsu's method on the b channel of the Lab color space to obtain pixels belonging to the nuclei (foreground pixels). In their Bayesian method, Naik et al. [15] obtained training pixels of three different tissue classes which are lumen, nucleus and cytoplasm. For each class ω_v , they learned a probability density function $p(c, f(c)|\omega_v)$ for a pixel c with color $f(c)$. By using Bayes Theorem, they computed the posterior probability $P(\omega_v|c, f(c))$ that each pixel c belongs to each class ω_v in the image. A pixel c is classified as nucleus if $P(\omega_N|c, f(c)) > T_N$ where ω_N denotes the nucleus class and T_N denotes a pre-defined threshold. Since we cannot estimate the threshold T_N being used in their method, we classify a pixel c as nucleus if $P(\omega_N|c, f(c)) > P(\omega_C|c, f(c))$ and $P(\omega_N|c, f(c)) > P(\omega_L|c, f(c))$, where ω_C and ω_L denote the cytoplasm and lumen classes, respectively. Similar to their work, we use 600 pixels per class for training. The results of the three methods are presented in Figure 7. It can be seen from these results that the proposed method gives more satisfactory outputs than the other two methods. While the Otsu method does not employ any domain knowledge and the Bayesian method may suffer from the high color variation of the tissue structures among images, the proposed method uses prior knowledge about nucleus features (which are mostly stable among images) and does not depend on color of some training pixels.

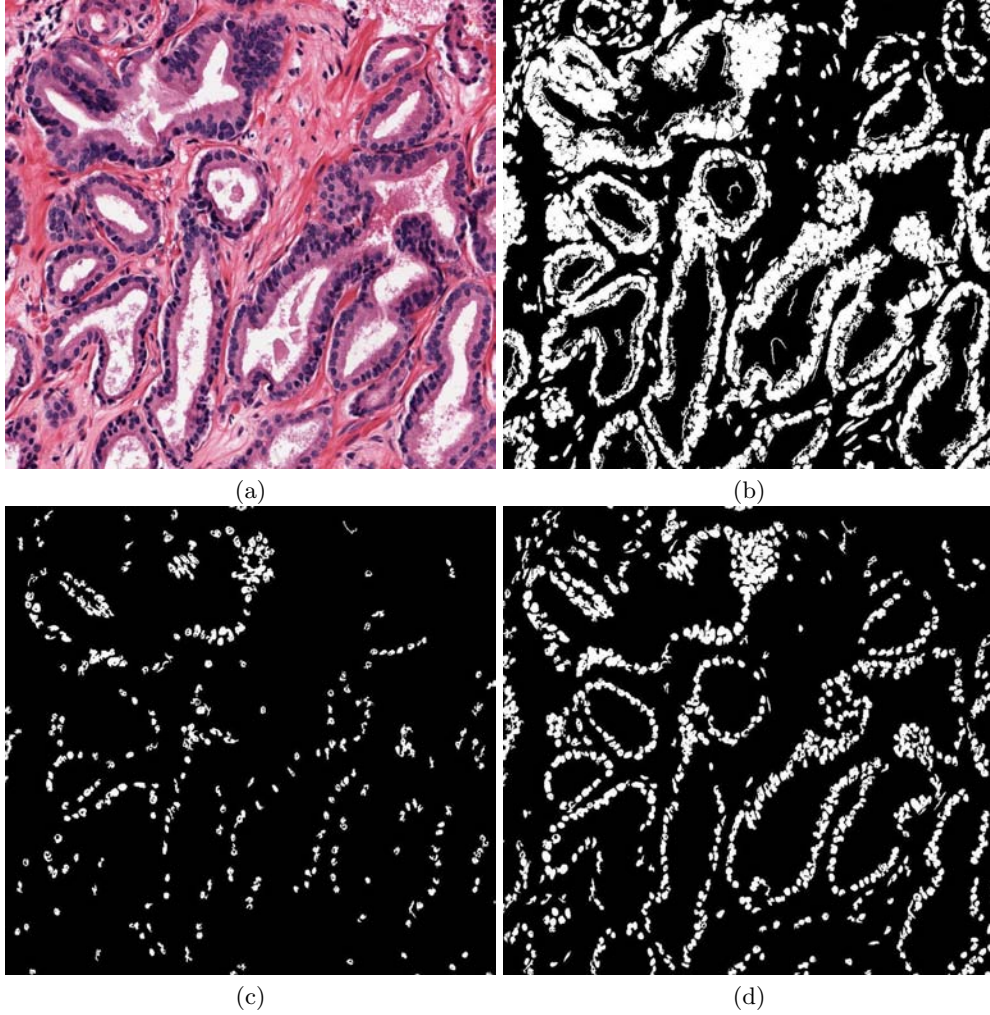


Fig. 7. Comparison of the three nucleus segmentation methods. (a) A sampled region of a whole slide image. (b) Result of the Otsu method. (c) Result of the Bayesian method. (d) Result of the proposed method.

We also analyze the computational complexity of the proposed nucleus segmentation algorithm by calculating the number of operations to be performed. There are three steps in the proposed algorithm: (i) thresholding the grayscale image with a threshold t , (ii) performing the connected component labeling using all image pixels and (iii) computing features of the objects (connected components). These three steps are repeated for all T threshold values in $[t_{min}, t_{max}]$. In the thresholding step, there are n comparisons for an image with n pixels, yielding a complexity of $\Theta(n)$. In the connected component labeling, by using a two-pass algorithm (every pixel is visited twice) with 4-connectivity at every pixel, $2 \times 4 \times n$ operations are needed, which corresponds to a complexity of $\Theta(n)$. To compute features (area and circularity) of each segmented object O_i with n_i points, we need to visit all the points and consider the 4 neighbors at every point to find the object perimeter, which results in $4n_i$ operations. The total number of operations for this step is $\sum_i 4n_i$, which corresponds to a complexity of $\Theta(\sum_i 4n_i) = \Theta(4n) = \Theta(n)$ (since $\sum_i n_i < n$). In summary, the final complexity of the algorithm is $T \times (\Theta(n) + \Theta(n) + \Theta(n)) = \Theta(n)$, which is linear in terms of the number of pixels in the image.

6 Conclusions

We have introduced a novel cytological feature for automated prostate cancer detection, which is different from the structural features used in the Gleason grading method. An efficient adaptive binarization approach is proposed to extract this cytological feature, namely the cancer nucleus feature. Though the Gleason grading method is widely used in grading prostate cancer, there is still a need to examine the tissue at a high magnification and utilize the cytological features to enhance the diagnosis results. For a computer aided system, besides the use of well-known textural features, we can also include the cancer nucleus feature in particular and cytological features in general to boost the performance of the system. The results achieved on the test images reported here demonstrate the contribution of the cancer nucleus feature in detecting prostate cancer. In future work, we intend to obtain a larger dataset and explore additional cytological features. Moreover, we plan to perform gland segmentation and use the outputs to facilitate cancer detection. This means we can process cancer detection at a higher level (glandular level) instead of patch-based classification which relies mainly on image pixels.

References

1. Kiernan, J.A.: *Histological and Histochemical Methods: Theory and Practice*. A Hodder Arnold Publication (2001)
2. Gleason, D.: Histologic grading and clinical staging of prostatic carcinoma. *Urologic Pathology: The Prostate*, M. Tannenbaum, Ed. Philadelphia, PA: Lea and Febiger (1977) 171–198
3. Nguyen, K., Jain, A., Allen, R.: Automated gland segmentation and classification for gleason grading of prostate tissue images. In: *Proc. International Conf. Pattern Recognition*. (2010) 1497–1500
4. Gong, Y., Caraway, N., Stewart, J., Staerkel, G.: Metastatic ductal adenocarcinoma of the prostate: cytologic features and clinical findings. *J. clin. Path.* **126** (2006) 302–309
5. Monaco, J.P., Tomaszewski, J.E., Feldman, M.D., Hagemann, I., Moradi, M., Mousavi, P., Boag, A., Davidson, C., Abolmaesumi, P., Madabhushi, A.: High-throughput detection of prostate cancer in histological sections using probabilistic pairwise markov models. *Medical Image Analysis* **14** (2010) 617–629
6. Doyle, S., Feldman, M., Tomaszewski, J., Madabhushi, A.: A boosted bayesian multi-resolution classifier for prostate cancer detection from digitized needle biopsies. *IEEE Transactions on Biomedical Engineering*. (1990) 581–590
7. Mason, M.: Cytology of the prostate. *J. clin. Path.* (1964) 581–590
8. Diaconescu, S., Diaconescu, D., Toma, S.: Nucleolar morphometry in prostate cancer. *Bulletin of the Transilvania University of Brasov* **3** (2010)
9. Diamond, J., Anderson, N., Bartels, P., Montironi, R., Hamilton, P.: The use of morphological characteristics and texture analysis in the identification of tissue composition in prostatic neoplasia. *Human Pathology* **35** (2004) 1121–1131
10. Khouzani, K.J., Zadeh, H.S.: Multiwavelet grading of pathological images of prostate. *IEEE Transactions on Biomedical Engineering* **50** (2003) 697–704
11. Tabesh, A., Teverovskiy, M., Pang, H.: Multifeature prostate cancer diagnosis and gleason grading of histological images. *IEEE Transactions on Medical Imaging* **26** (2007) 1366–1378
12. Haralick, R., Shanmugam, K., Dinstein, I.: Textural features for image classification. *IEEE Trans. Syst. Man Cybern. SMC* **3** (1973) 610–621
13. Jain, A.K., Farrokhnia, F.: Unsupervised texture segmentation using gabor filters. *Pattern Recognition* **24** (1991) 1167–1186
14. Otsu, N.: A threshold selection method from gray-level histograms. *IEEE Trans. Sys., Man., Cyber* **9** (1979) 62–66
15. Naik, S., Doyle, S., Feldman, M., Tomaszewski, J., Madabhushi, A.: Gland segmentation and computerized gleason grading of prostate histology by integrating low-, high-level and domain specific information. *MIAAB Workshop* (2007)